Supporting Information

Manipulating the d-Band centers of transition metal phosphide through dual metal doping towards robust overall water splitting

Yunqing Liu,[‡][a] Zuhao Zhang,[‡][a] Lu Zhang,[a] Yuguo Xia,[b] Haiqing Wang,[*][a] Hong Liu,[*][a,c] Shenguang Ge,[*][a] and Jinghua Yu[d]

[a] Institute for Advanced Interdisciplinary Research, University of Jinan, Jinan 250022, China

[b] School of Chemistry and Chemical Engineering, Shandong University, Jinan 250100, China

[c] State Key Laboratory of Crystal Materials, Shandong University, Jinan 250100, China

[d] School of Chemistry and Chemical Engineering, University of Jinan, Jinan 250022, China

‡ These authors contributed equally to this work.

*Corresponding authors:

Haiqing Wang, E-mail: ifc_wanghq@ujn.edu.cn

Hong Liu, E-mail: hongliu@sdu.edu.cn

Shenguang Ge, E-mail: chm_gesg@163.com

1. Experimental section

1.1 Characterizations

Surface morphologies of as-prepared samples were characterized by field-emission scanning electron microscopy (SEM, TESCAN MIRA4). Transmission electron microscopy (TEM) and high-resolution transmission electron microscopy (HRTEM) images and energy-disperse X-ray spectra (EDX) elemental mapping spectra were recorded with Talos F200x. X-ray diffraction (XRD) patterns were measured by using SmartlabSE X-ray diffractometer. X-ray photoelectron spectra (XPS) were recorded by Thermo Scientific K-Alpha with Al Ka radiation (hv=1486.6eV).

1.2 Electrochemical Measurements

All electrocatalytic measurements were performed with a Chenhua CHI760E instrument in 1 M KOH media, at room temperature. In a typical three-electrode configuration, the as-prepared samples were used directly as working electrodes with an area of 0.5×0.5 cm^2, while a Hg/HgO electrode and a graphite rod were utilized as the reference and counter electrodes, respectively. The electrocatalytic performance toward OER and HER of as-prepared samples were determined by using linear sweep voltammetry (LSV) at a scan rate of 1 mV s^{-1}, 95% IR compensation. Overall water splitting was performed in a typical two-electrode system with the as-prepared electrodes utilized as cathode and anode simultaneously. The electrochemical impedance spectroscopy (EIS) was employed in the frequency range of 100 kHz – 0.1 Hz at 1.53 V and -0.2 V vs. RHE for OER and HER, respectively. The stability of catalysts was tested by using chronopotentiometry at a current density of 500 mA cm^{-2} for OER, HER and overall water splitting. Faradaic efficiency for OER and HER was calculated by the water drainage method. Commercial Pt/C (20%,) and RuO$_2$ loaded on NiFe foam with a loading mass of 1.6 mg cm^{-2} were used as benchmark electrodes for HER and OER catalysis, respectively.

The electrochemical double-layer capacitance (C_{dl}) was calculated as half of the linear slope of the function by plotting the current density differences versus scan rates

(20, 40, 60, 80 and 100 mv s^{-1}) in non-Faradaic region. The ECSA was calculated according to the following equation:

$$ECSA = C_{dl}/C_s$$

In which C_s is the specific capacitance, commonly reported to be 40 µF cm^{-2}.[1-3]

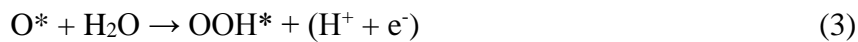The turnover frequency (TOF) of involved catalysts was calculated according to the following equation:

$$TOF = (J \times A)/(m \times F \times n)$$

In which J is the current density at the selected overpotential (250 mV for OER and 150 mV for HER), A is the surface area of the electrode (0.25 cm^2), m represents the number of mols of electrons for per mol of O_2 (4) or H_2 (2), F is the Faraday constant (96485.3 C mol^{-1}), and n is the number of active sites calculated according to the loading weight and the molecular weight.[4]

1.3 DFT calculations

DFT calculations corrected by onsite Coulomb interaction were performed using the Vienna ab initio simulation package (VASP). The exchange-correction function was treated by the Perdew−Burke−Ernzerhof for solid (PBEsol) generalized gradient approximation, and the wave functions were expanded in a plane wave basis with an energy cutoff of 400 eV. The effective U−J values of 3.5, 6.2, and 3.9 eV were introduced to account for the strong onsite Coulomb repulsion of Fe, Ni, and Mn atoms, respectively. The Brillouin zone was sampled by a gamma centered method. For all the calculations, the convergence criteria for the electronic and ionic relaxations are 10^{-5} eV and 0.02 eV/Å, respectively.

The four electrons pathway for OER process involves the following elementary steps:

$$* + H_2O \rightarrow OH^* + (H^+ + e^-) \qquad (1)$$

$$OH^* \rightarrow O^* + (H^+ + e^-) \qquad (2)$$

$$O^* + H_2O \rightarrow OOH^* + (H^+ + e^-) \qquad (3)$$

$$OOH^* \rightarrow * + O_2 + (H^+ + e^-) \qquad (4)$$

Where the * represents the active site on the catalyst surface, and O*, OH*, and OOH* represent the intermediates during the elementary steps of OER process. For each step, the Gibbs free energy change (ΔG) can be calculated according to the equation:

$$\Delta G = \Delta E + \Delta ZPE - T\Delta S \qquad (5)$$

Where the ΔE is the reaction energy of reaction and product molecules absorbed on catalyst surface, ΔZPE is the energy change in zero point energy, T equals to 298.15 K and ΔS is the entropy change.[5]

The Gibbs free energy change of adsorbed H (ΔG_{H*}) on different sites are calculated as:

$$\Delta G_{H*} = \Delta E_{H*} + \Delta ZPE - T\Delta S \qquad (6)$$

where ΔE_{H*} is the adsorption energy of H species on catalyst surface. ΔZPE is the energy change in zero point energy, T equals to 298.15 K and ΔS is the entropy change.[6]
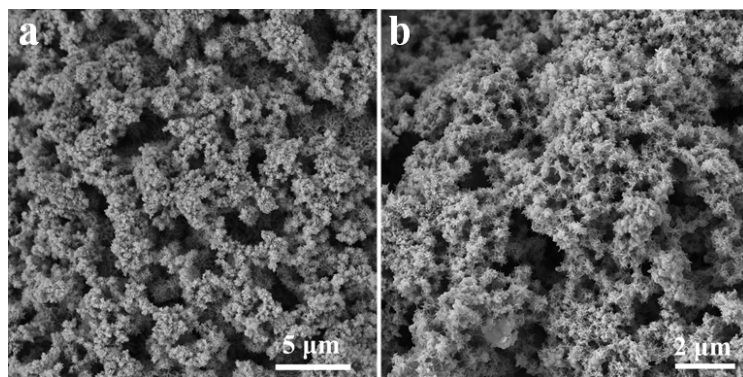
Fig. S1 SEM images of Ni-Mn-FeP (a, b).
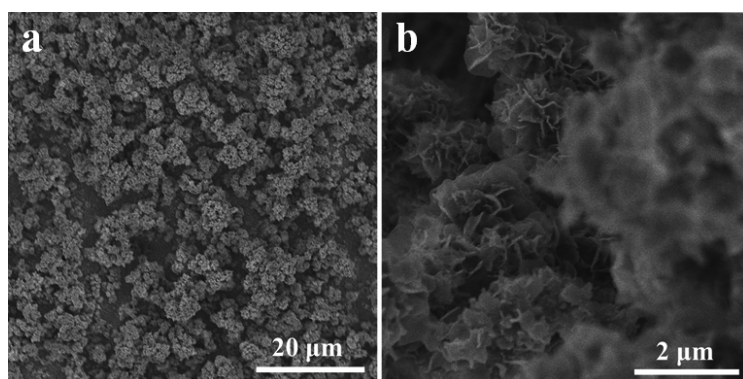
Fig. S2 SEM images of Ni-FeP (a, b).
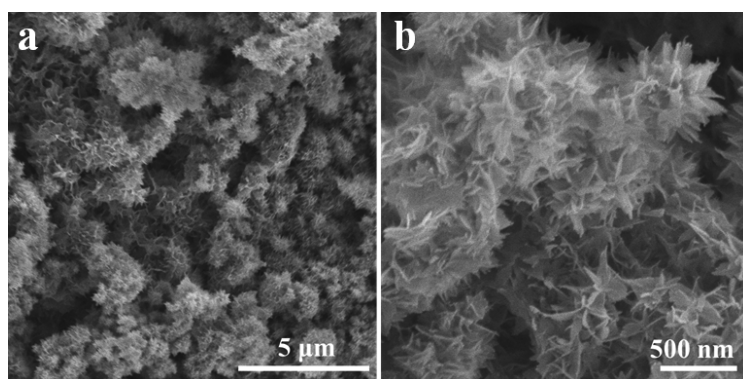
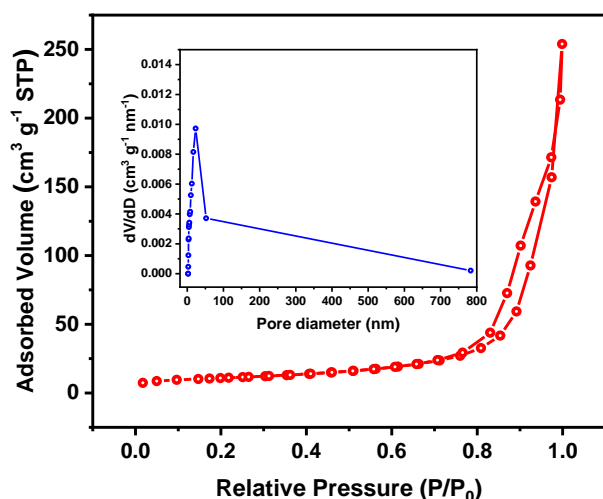Fig. S3 SEM images of Ni-Mn-FeOH (a, b).

Fig. S4 N_2 adsorption/desorption isotherm and the pore-size distribution curve (inset) of Ni-Mn-FeP.

The BET specific surface area of Ni-Mn-FeP had been measured to be 32.7 m^2 g^{-1}, with a most probable pore size of 23.23 nm and a pore volume of 0.40 cm^3 g^{-1}.
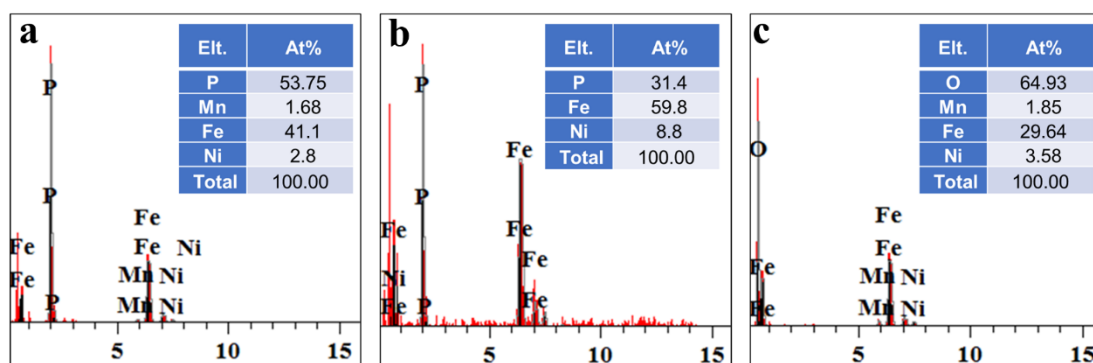

Fig. S5 EDS elemental spectra of Ni-Mn-FeP (a), Ni -FeP (b) and Ni-Mn-FeOH (c).

The atomic ratio of Ni, Mn and Fe in the Ni-Mn-FeP is displayed in Fig S5. It can be observed that the atomic ratio of metal and phosphorus is 46.25 to 53.75, close to the stoichiometric ratio of FeP. The atomic ratio of Ni, Mn and Fe is 2.8: 1.68: 41.1, indicating that FeP is the main phase.
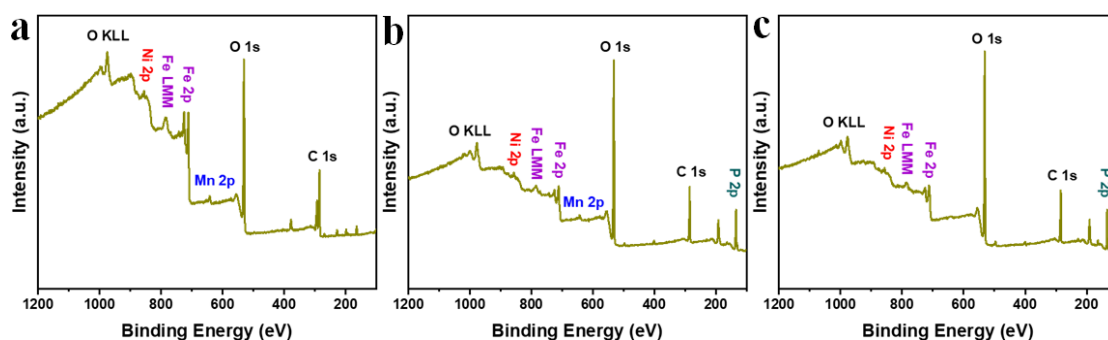
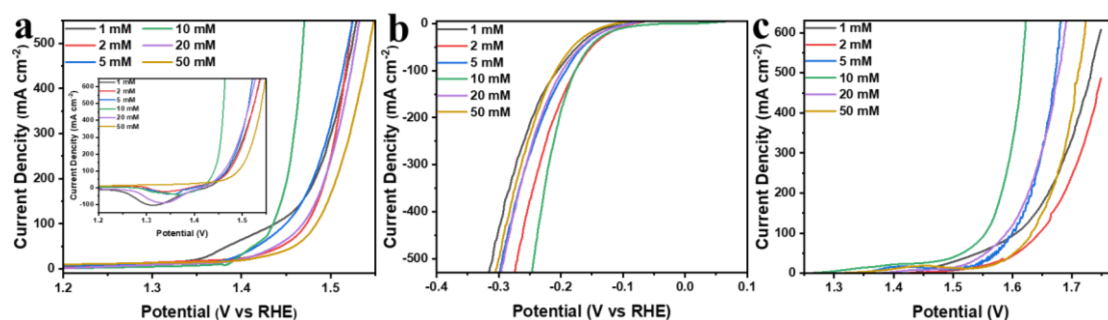Fig. S6 XPS survey spectra of Ni-Mn-FeOH (a), Ni-Mn-FeP (b) and Ni-FeP (c).

Fig. S7 LSV curves of Ni-Mn-FeP with different Mn contens for OER (a, inset: reverse LSV curves for OER), HER (b) and overall water splitting (c) in 1 M KOH.

By adjusting the concentration of Mn^{2+} in the etching solution, we had prepared series of catalysts with different Mn contents and tested their electrocatalytic performance, as shown in Fig. S7. For the catalysts prepared with the Mn^{2+} concentration of 1, 2, 5, 10, 20, 50 mM, the overpotential at 10 mA cm^{-2} for OER are 202, 197, 190, 185, 193 and 223 mV. The overpotential at 10 mA cm^{-2} for HER are 132, 109, 117, 103, 120, 142 mV. For verall water splitting, the cell voltage for 100 mA cm^{-2} are 1.61, 1.64, 1.60, 1.55, 1.59 and 1.63 V. It can be observed that the catalyst prepared with 10 mM Mn^{2+}, with a Mn atomic ratio of 1.68 % exhibits the best performance toward HER, OER and overall water splitting.
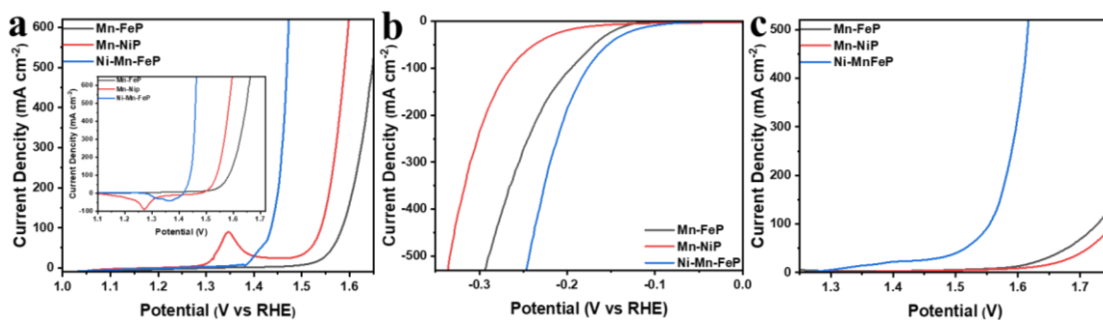
Fig. S8 LSV curves of Ni-Mn-FeP, Mn-FeP and Mn-NiP for OER (a, inset: reverse LSV curves for OER)), HER (b) and overall water splitting (c) in 1 M KOH.

Ni foam and Fe foam had been used as substrates for the preparation of catalysts. The electrocatalytic performance had been tested and provided in Fig. S8. It can be observed in Fig S8a, Ni-Mn-FeP requires an overpotential of 185 mV to deliver a current density of 10 mA cm^{-2}, which is 83 and 95 mV smaller than that of Mn-NiP and Mn-FeP, respectively. For HER, as shown in Fig. S8b, the overpotential at 10 mA cm^{-2} for Ni-Mn-FeP, Mn-NiP and Mn-FeP are 103, 173 and 134 mV, respectively. When used as both anode and cathode for water splitting, the advantage of catalytic performance for Ni-Mn-FeP is more obvious. According to the catalytic performance comparison toward OER, HER and overall water splitting, the interaction between Ni and Fe also makes great contributions to the superior catalytic performance toward OER and HER.
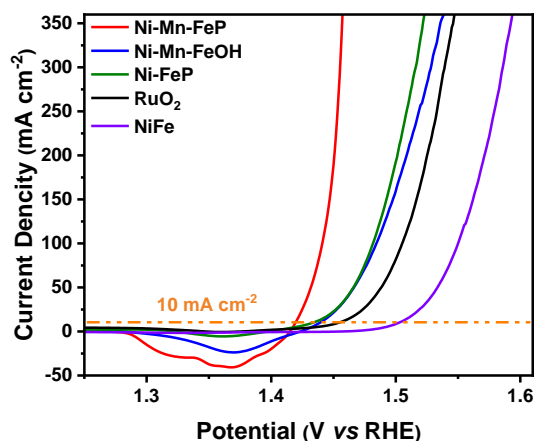

Fig. S9 Reverse LSV curves of Ni-Mn-FeP, Ni-FeP, Ni-Mn-FeP, RuO_2 and NiFe for OER in 1 M KOH.

Reverse LSV scan had been provided in Fig. S9. The overpotential at 10 mA cm^{-2}

for Ni-Mn-FeP, Ni-Mn-FeOH, Ni-FeP and RuO$_2$ had been corrected to be 185 mV, 211 mV, 206 mV and 228 mV, respectively. The difference between the positive LSV curve and the reverse LSV curve can be attributed to the oxidation of the catalysts.
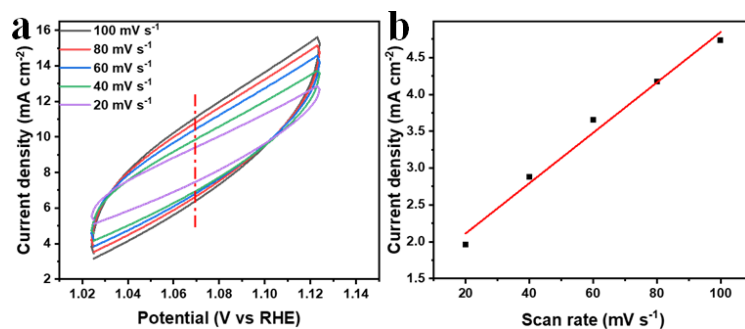

Fig. S10 (a) CV curves of Ni-Mn-FeP at different scan rate. (b) C$_{dl}$ calculations with capacitive current as a function of scan rate.
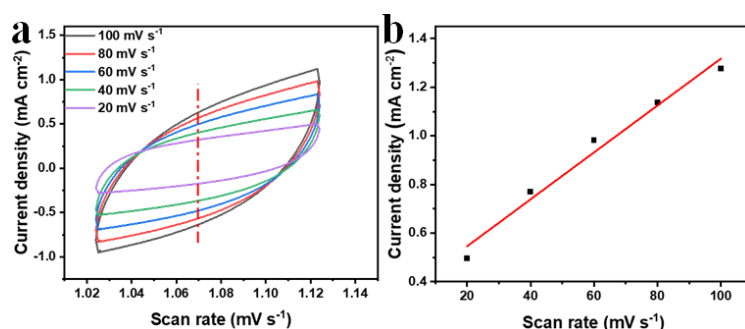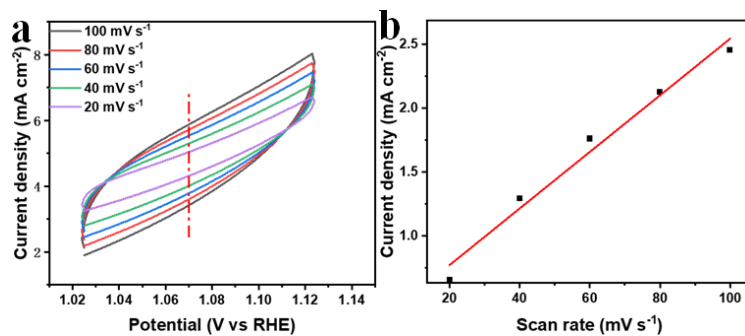

Fig. S11 (a) CV curves of Ni-Mn-FeOH at different scan rate. (b) C$_{dl}$ calculations with capacitive current as a function of scan rate.

Fig. S12 (a) CV curves of Ni-FeP. at different scan rate. (b) C$_{dl}$ calculations with capacitive current as a function of scan rate.
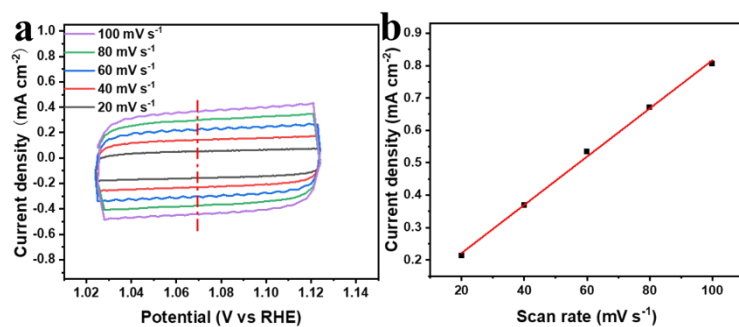
Fig. S13 (a) CV curves of NiFe at different scan rate. (b) C_{dl} calculations with capacitive current as a function of scan rate.
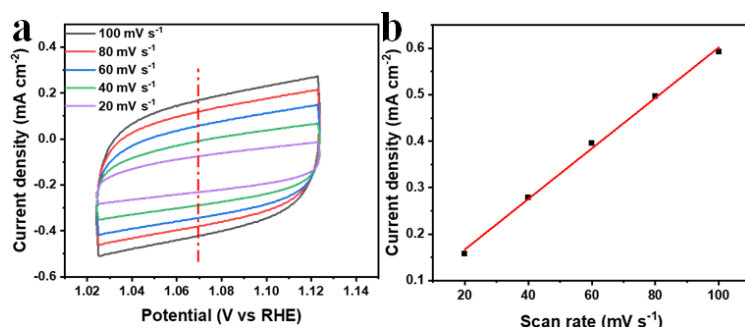

Fig. S14 (a) CV curves of RuO_2 at different scan rate. (b) C_{dl} calculations with capacitive current as a function of scan rate.
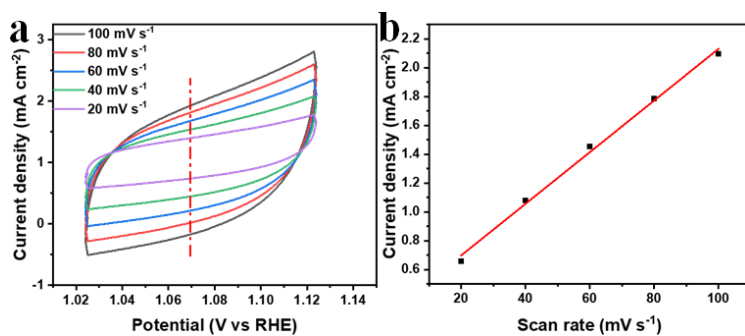

Fig. S15 (a) CV curves of Pt/C at different scan rate. (b) C_{dl} calculations with capacitive current as a function of scan rate.
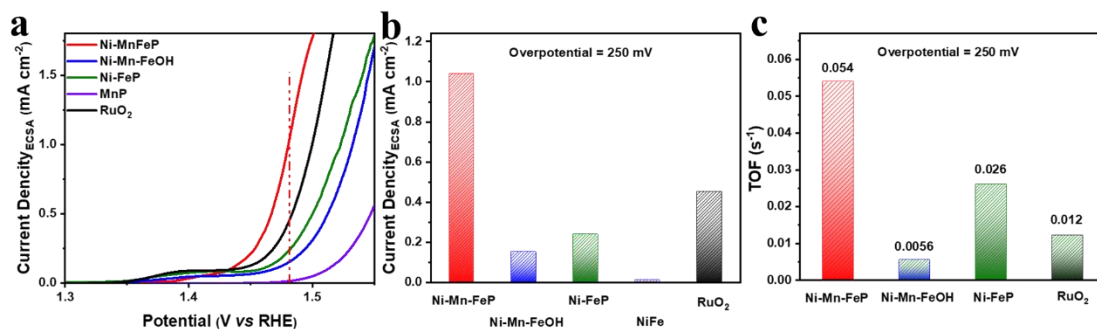
Fig. S16 (a) ECSA normalized LSV curves for OER. (b) ECSA normalized current density at the overpotential of 250 mV. (c) TOFs for OER at the overpotential of 250 mV.
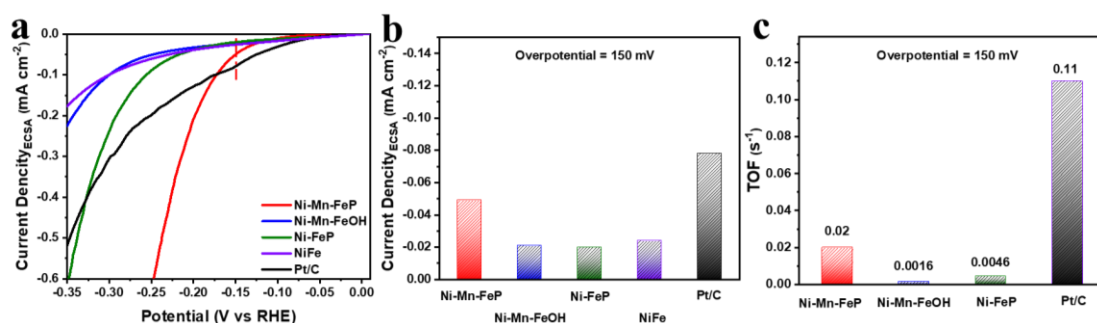

Fig. S17 (a) ECSA normalized LSV curves for HER. (b) ECSA normalized current density at the overpotential of 150 mV. (c) TOFs for HER at the overpotential of 150 mV.
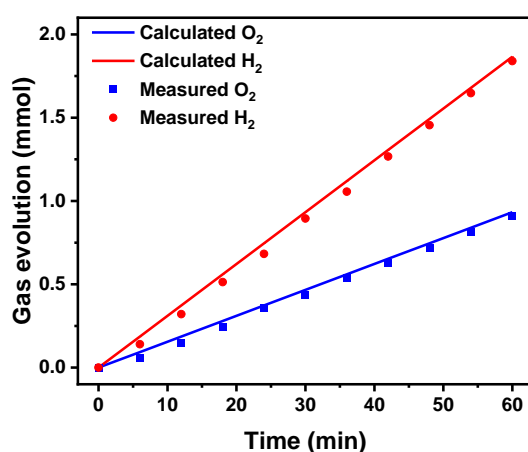

Fig. S18 The amount of O_2 and H_2 theoretically calculated and experimentally measured versus time for Ni-Mn-FeP at 100 mA for 60 min.

The faradaic efficiency (FE) was measured by the water-drainage experiment, which was performed in a sealed H-type cell, with Ni-Mn-FeP used as both cathodic and

anodic electrodes, respectively. The test was conducted at a current of 100 mA for 60 min. The gas volumes of H_2 and O_2 generated were recorded every 6 min. The Faraday Efficiency was calculated according to the following equation:

$$FE = V*n*F/I*t*22.4$$

In which the V is the volume of the generated O_2 or H_2 (L). n represents the number of mols of electrons for per mol of O_2 (4) or H_2 (2). F is the Faraday constant (96485.3 C mol^{-1}). I is the current (0.1 A) and t is the test time (s). Faradic efficiency for OER and HER had been calculated to be 97.3% and 98.6% respectively.
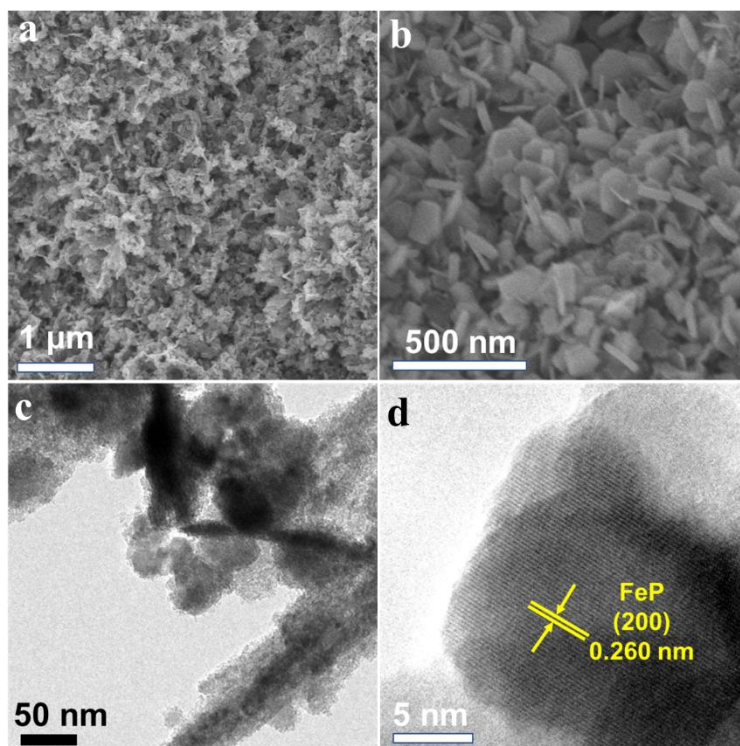

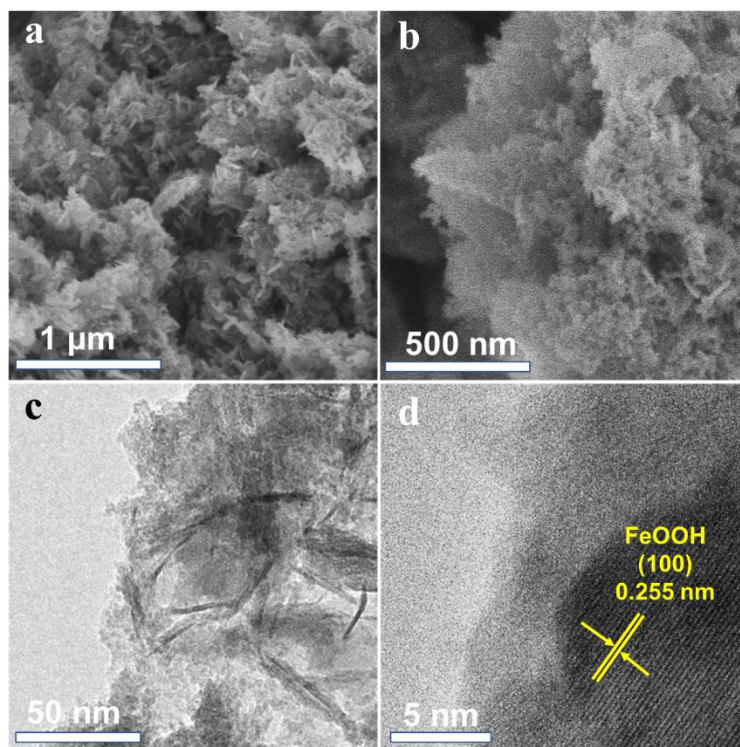Fig. S19 SEM images (a, b) and TEM images (c, d) of post-HER Ni-Mn-FeP.

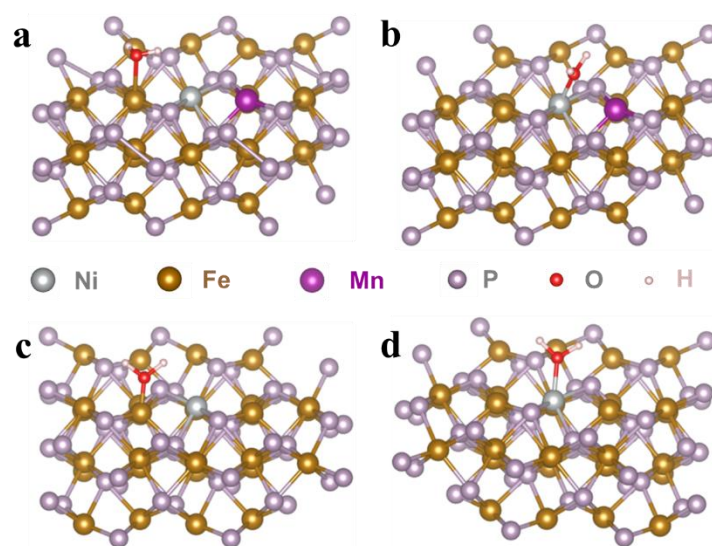Fig. S20 SEM images (a, b) and TEM images (c, d) of post-OER Ni-Mn-FeP.

Fig. S21 Calculated H_2O adsorption models on Fe (a), Ni (b) sites of Ni-Mn-FeP and Fe (c), Ni (d) sites of Ni-FeP.
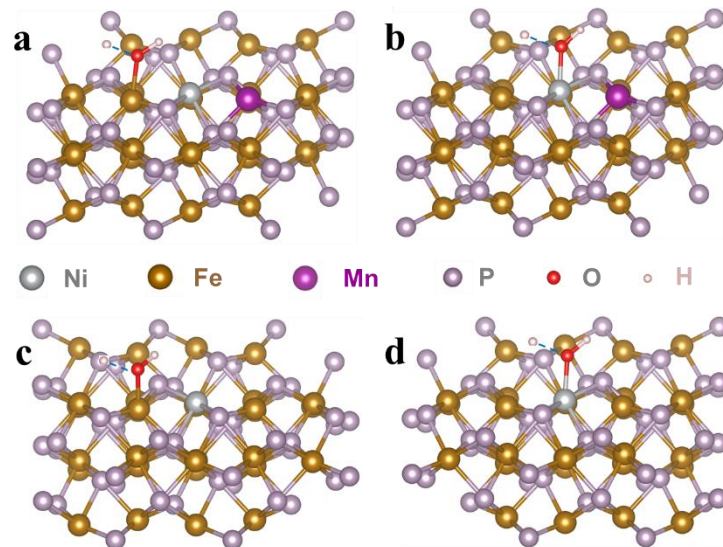
Fig. S22 Calculated *H-*OH adsorption models on Fe (a), Ni (b) sites of Ni-Mn-FeP and Fe (c), Ni (d) sites of Ni-FeP.

Fig. S23 Calculated H adsorption models on Fe (a), Ni (b) sites of Ni-Mn-FeP and Fe (c), Ni (d) sites of Ni-FeP.

Fig. S24 Calculated *OH adsorption models on Fe (a), Ni (b) sites of Ni-Mn-FeP and Fe (c), Ni (d) sites of Ni-FeP.

Fig. S25 Calculated *O adsorption models on Fe (a), Ni (b) sites of Ni-Mn-FeP and Fe (c), Ni (d) sites of Ni-FeP.

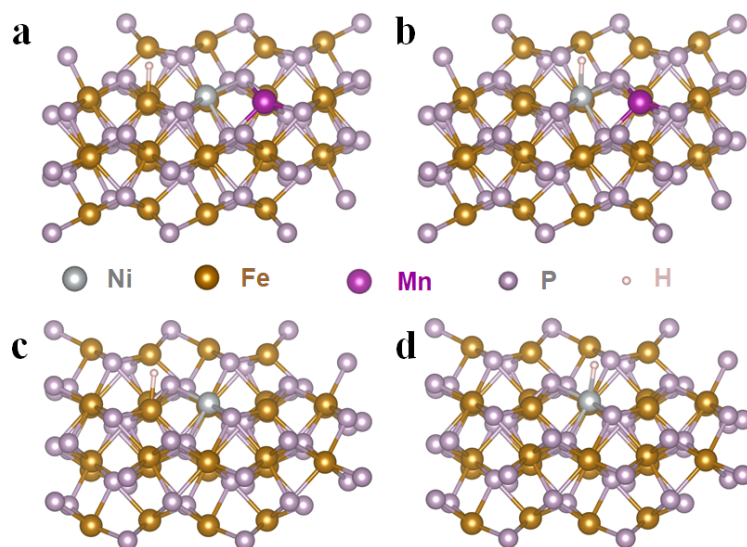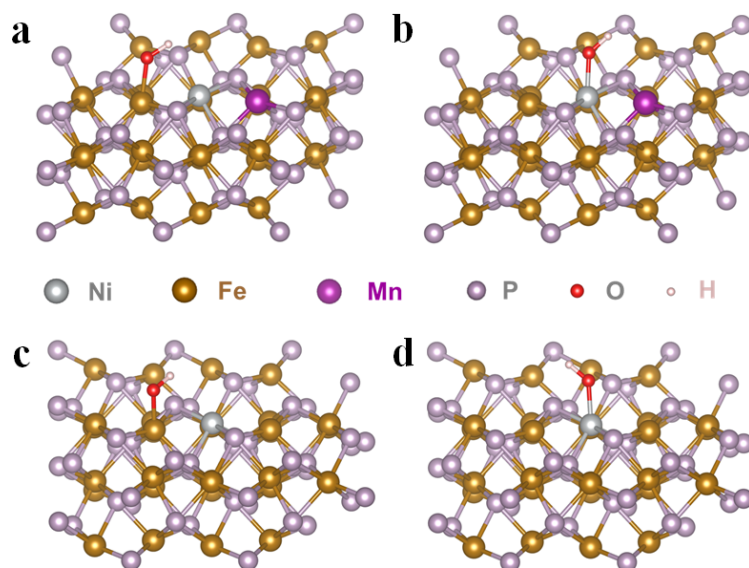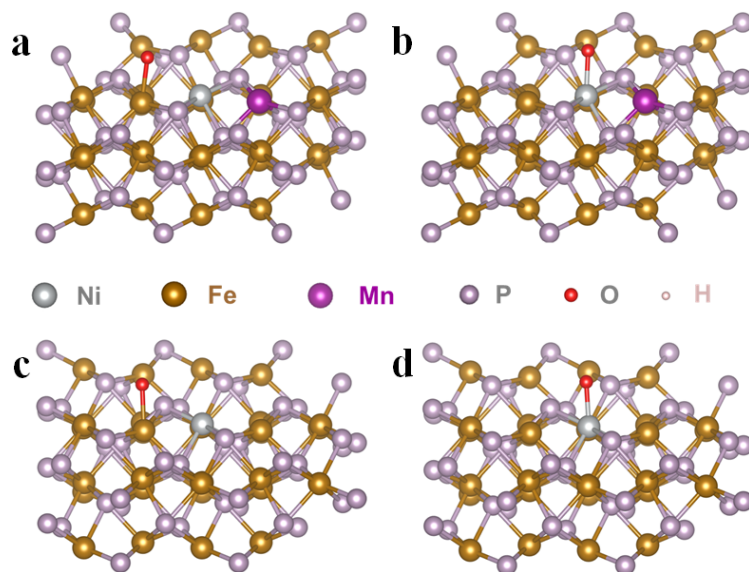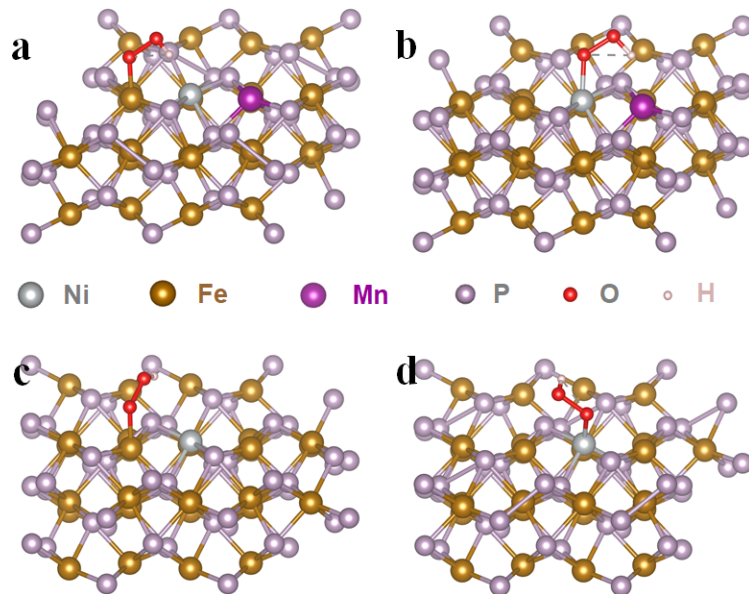Fig. S26 Calculated *OOH adsorption models on Fe (a), Ni (b) sites of Ni-Mn-FeP and Fe (c), Ni (d) sites of Ni-FeP.
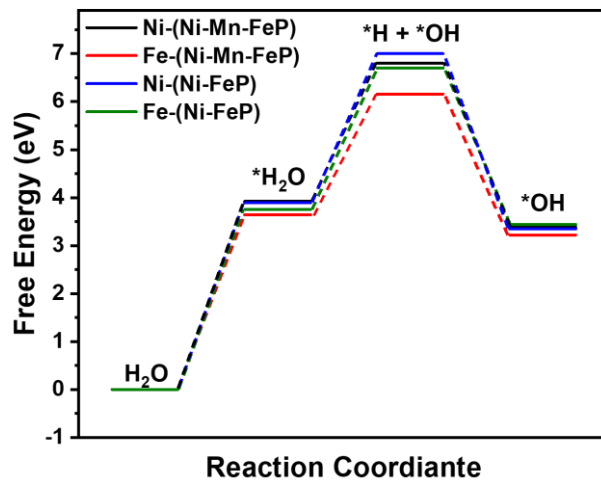
Fig. S27 Calculated free energy diagrams of the HER pathways on Fe, Ni sites of Ni-Mn-FeP and Fe, Ni sites of Ni-FeP.

Table S1 The Gibbs free energy changes (ΔG) of the elementary steps during OER process.

Catalytic sites	ΔG_I (* → *OH)	ΔG_{II} (*OH → *O)	ΔG_{III} (*O →*OOH)	ΔG_{IV} (*OOH → *)
Ni-(Ni-Mn-FeP)	-0.226 eV	0.278 eV	3.045 eV	1.620 eV
Fe-(Ni-Mn-FeP)	0.151 eV	-0.141 eV	3.572 eV	1.338 eV
Ni-(Ni-FeP)	-0.124 eV	0.379 eV	4.166 eV	0.498 eV
Fe-(Ni-FeP)	0.550 eV	-0.491 eV	3.521 eV	1.340 eV

Table S2 Comparation of the recently reported transition metal phosphates based bifunctional electrocatalyst for water splitting.

Catalysts	Overpotential for OER (mV)		Overpotential for HER (mV)		Cell voltage (V)	Ref
	η_{10}	Tafel slope (mV dec^{-1})	η_{10}	Tafel slope (mV dec^{-1})	η_{10}	
Ni-Mn-FeP	185	49.4	103	71.6	1.48	This work
amorphous FeP-Ni/NF	218	60	120	112	1.62	[7]
(Fe$_{0.14}$Ni$_{0.47}$Co$_{0.39}$)$_2$P/CFP	230	77	90	98	1.59	[8]
NiCoVP/NiFeVP	234	34.4	42	30	1.50	[9]
NiFeP/SG	218	44	115	47	1.54	[10]
CoP@NPCSs	350	103	115	70	1.643	[11]
Sn$_4$P$_3$/Co$_2$P	280.4	52.7	45.4	72.8	1.56	[12]
Co$_4$Ni$_1$P	245	61	129	52	1.59	[13]
iron/nickel phosphides	185	47	63	59	1.567	[14]
hollow CoFeP	350	59	157	72	1.57	[15]
Co@CoP$_2$/CF	210	95	55	62	1.54	[16]

References

1   W. Yan, Y. Shen, C. An, L. Li, R. Si, C. An, *Appl. Catal. B-Environ., 2021, 284, 119687.*

2   F. Qin, Z. Zhao, M.K. Alam, Y. Ni, F. Robles-Hernandez, L. Yu, S. Chen, Z. Ren, Z. Wang, J. Bao, *ACS Energy Lett.*, 2018, **3**, 546–554.

3   P. Liu, X. Li, S. Yang, M. Zu, P. Liu, B. Z, L. Zheng, H. Zhao, H. Yang, *ACS Energy Lett.*, 2017, **2**, 2257−2263.

4   P. Li, X. Duan, Y. Kuang, Y. Li, G. Zhang, W. Liu, X. Sun, *Adv. Energy Mater.*, 2018, **8**, 1703341.

5   H. Wang, Y. Xia, H. Li, X. Wang, Y. Yu, X. Jiao and D. Chen, *Nat. Commun.*, 2020, **11**, 3078.

6   J.-S. Li, Y. Wang, C.-H. Liu, S.-L. Li, Y.-G. Wang, L.-Z. Dong, Z.-H. Dai, Y.-F. Li and Y.-Q. Lan, *Nat. Commun.*, 2016, **7**, 112014.

7   G. Liu, Y. Wu, R. Yao, F. Zhao, Q. Zhao and J. Li, *Green Energy Environ.*, 2021, **6**, 496-505.

8   L. Pang, W. Liu, X. Zhao, M. Zhou, J. Qin and J. Yang, *ChemElectroChem*, 2020, **7**, 4913.

9   Y. Jeung, H. Jung, D. Kim, H. Roh, C. Lim, J. Han and K. Yong, *J. Mater. Chem. A*, 2021, **9**, 12203-12213.

10 R. Li, B. Wang, T. Gao, R. Zhang, C. Xu, X. Jiang, J. Zeng, Y. Bando, P. Hu, Y. Li and X. Wang, *Nano Energy*, 2019, **58**, 870–876.

11 K. Wu, Z. Chen, W. Cheong, S. Liu, W. Zhu, X. Cao, K. Sun, Y. Lin, L. Zheng, W. Yan, Y. Pan, D. Wang, Q. Peng, C. Chen and Y. Li, *ACS Appl. Mater. Interfaces*, 2018, **10**, 44201−44208.

12 X. Qin, B. Yan, D. Kim, Z. Teng, T. Chen, J. Choi, L. Xu and Y. Piao, *Appl. Catal. B Environ.*, 2022, **304**, 120923.

13 L. Yan, L. Cao, P. Dai, X. Gu, D. Liu, L. Li, Y. Wang and X. Zhao, *Adv. Funct. Mater.*, 2017, **27**, 1703455.

14 X. Xu, X. Tian, Z. Zhong, L. Kang and J. Yao, *J. Power Sources*, 2019, **424**, 42–51.

15 Y. Du, H. Qu, Y. Liu, Y. Han, L. Wang and B. Dong, *Appl. Surf. Sci.*, 2019, **465**, 816-823.

16 Y. Sun, T. Liu, Z. Li, A. Meng, G. Li, L. Wang and S. Li, *Chem. Eng. J.*, 2022, **433**, 133684.